High Temperature Corrosion of Materials
https://doi.org/10.1007/s11085-024-10304-4

ORIGINAL PAPER

Hot Corrosion Behaviour by Na_2SO_4 Deposits of the 1st Generation AM1 Single-Crystal Nickel-Based Superalloy at 750 °C

D. Piel[1] · A. Martin[1,2,3] · E. Drouelle[2] · J. Cormier[3] · F. Pedraza[1]

Received: 15 August 2024 / Revised: 15 August 2024 / Accepted: 26 August 2024

Abstract

This paper highlights that hot corrosion at 750 °C can develop on the surface of AM1 nickel-based single-crystal superalloy (SX) turbine blades, whether in the As-Cast (AC) or Fully Heat-Treated (FHT) states even in the absence of SO_3 (g) flow. It was found that the 1 and 3 mg/cm^2 Na_2SO_4 deposits induce sulphidation, oxidation and basic flux at such low temperature like in Type I hot corrosion. Sulphidation is mainly located in the γ'-depleted zone irrespective the substrate (AC and FHT). The metallurgical segregations in the AC superalloy extend the incubation period in contrast to what is observed upon pure oxidation. The increase in salt content showed a reduction in hot corrosive attack by forming a barrier layer.

Keywords Single-crystal nickel-based superalloy · As-cast materials · Hot corrosion · Sodium sulphate

✉ D. Piel
damien.piel@univ-lr.fr

A. Martin
angeline.martin@safrangroup.com

E. Drouelle
elodie.drouelle@safrangroup.com

J. Cormier
jonathan.cormier@ensma.fr

F. Pedraza
fpedraza@univ-lr.fr

[1] Laboratoire des Sciences de l'Ingénieur pour l'Environnement (LaSIE, UMR-CNRS 7356), La Rochelle Université, Avenue Michel Crépeau. 17042, La Rochelle cedex 1, France

[2] Safran Aircraft Engines, 171 boulevard de Valmy, 92700 Colombes, France

[3] ISAE-ENSMA, Institut Pprime, UPR CNRS 3346, 1 avenue Clément Ader, 86961 Futuroscope—Chasseneuil, France

Published online: 19 September 2024

Introduction

Nickel-based single-crystal (SX) superalloys are widely used materials in the production of turbine blades for the aerospace industry due to their excellent mechanical properties (fatigue, creep) at high temperatures [1]. Nevertheless, the service life of these components is often limited by the hot corrosion behaviour of uncoated gas turbine components owing to harmful conditions such as the presence of sodium sulphate (Na_2SO_4) [2–4]. Indeed, Na_2SO_4 is the most representative salt deposit of this degradation phenomenon and is linked to the reaction of sodium chloride (NaCl) from marine environments ingested by the engine with sulphur oxides (SO_2, SO_3) formed during the combustion of kerosene or the overflight of industrial areas. Different degradation mechanisms can then be identified, depending on the specific temperature range, such as pitting (Type II) or relatively homogeneous attacks (Type I) that can lead to the appearance of cracks and the reduction of the metal cross-section [5]. These two corrosive modes are kinetically characterized by an initiation stage (slow degradation) and a propagation stage (acceleration of corrosion) [6]. While Type I often occurs once Na_2SO_4 is molten [7], Type II hot corrosion is observed at temperatures below the melting temperature of Na_2SO_4 ($T_m = 884$ °C). As described by Meier [8] and Luthra [9, 10], the materials degrades by reaction between the salt deposited in solid form and the oxide layer formed and requires a sufficient amount of SO_3 that Wang et al. reported to be as low as 100 ppm for the corrosion of NiAl by Na_2SO_4-K_2SO_4 at 700 °C [11]. The critical SO_3 content may vary depending mostly on the substrate as recently reported by Malacarne et al. [12] provided that the $SO_2 + 1/2\ O_2$ reaction leading to SO_3 is efficiently catalysed by e.g., Pt or Fe catalysts or the active surface of the Na_2SO_4 solid itself or other elements of the alloy [13]. In Type II hot corrosion, the oxides like NiO or CoO react first to form their respective sulphates and then, eutectic phases by reaction with solid Na_2SO_4 [14]. This lowers the melting temperature to 671 °C and 578 °C for Na_2SO_4-$NiSO_4$ and Na_2SO_4-$CoSO_4$ mixtures, respectively [15, 16]. However, the influence of Na_2SO_4 without SO_3 has almost never been discussed before, even though J. Stringer reported that Type I can be observed at temperatures as low as 750 °C, and perhaps lower [17] but the reasons for this to occur were not developed although it is known that SO_2 (leading to SO_3) is not permanently present in the hot gas coming out of the combustion chamber or in the purged cooling air of the compressor. Therefore, this study intends to elucidate whether hot corrosion occurs at such low temperatures by comparing with air oxidation on a 1st generation AM1 nickel-based single-crystal superalloy. Two different salt deposits are applied with the goal of determining the exclusive contribution that the Na_2SO_4 salt may exert. A comparison is also established between the As-Cast (AC) and fully homogenized (FHT) microstructures to highlight the chemical segregation effects.

Experimental Procedure

The AM1 superalloy, whose chemical composition is shown in Table 1, was supplied by Safran Aircraft Engines (SAE). This first-generation nickel-based monocrystalline superalloy was cast in the form of rods approximately 20 mm in diameter in the direction < 001 > [18, 19]. After solidification, some of the material in As-Cast (AC) AM1 underwent a full heat treatment (FHT). This additional step includes solution treatment at 1300 °C for 3 h, followed by ageing at 1100 °C for 5 h, and then ageing at 870 °C for 16 h, with air quenching between each processing step. The resulting materials have a specific γ/γ' microstructure comprising dendrites, interdendritic spaces and eutectic pools. This characteristic is clearly observed in the case of the AC material with more irregular and coarser γ' precipitates in the interdendritic zone. However, the structural morphology of the FHT material is more difficult to discern due to homogenization to reduce chemical segregation and eutectic pools to optimize mechanical properties [20–22].

The rods were then cut perpendicular to the direction of solidification to obtain circular specimens approximately 1 mm thick and 10 mm in diameter. Before exposure, each sample was gently and gradually polished with SiC sandpaper up to grade P1200 in order to reduce the residual stresses induced during cutting. The specimens were then cleaned with acetone and ethanol in an ultrasonic bath before being weighed with a $\pm 10^{-5}$ g accurate balance. For the corrosion tests only, two separate deposits of sodium sulphate (1.0 ± 0.3 and 3.0 ± 0.3 mg/cm^2) were evenly sprayed onto the surface of AM1 from a saturated aqueous solution. This deposit was renewed every 24 h according to the ISO 17224 standard [23]. The oxidation and corrosion tests were performed in a Carbolite XCWF 1300X muffle furnace and a Pyrox resistive furnace, respectively, at an isothermal temperature of 750 °C under air (1 atm.) at varying times (5, 30 min, 1, 10, 24, 48, 96, 144, and 240 h). To increase the reproducibility of the experiments, two samples were introduced for all tests. After exposure, the samples were examined by Leica DMRM optical microscope to analyse the surface and cross-sections at different magnifications. The composition and crystal structure of the oxidized phases were obtained by combining the use of Raman spectroscopy (Jobin–Yvon Labram HR Evolution, $\lambda = 532$ nm), X-ray diffraction, XRD (Bruker AXS D8, $\lambda = K\alpha Cu$) and fluorescence spectroscopy (Bruker Tornado M4, $\lambda = K\alpha Rh$). Further detailed analyses were performed by Energy Dispersive Spectrometry (EDS) with an EDAX detector coupled to a FEI Quanta 200-F Scanning Electron Microscope (SEM) operating systematically at 20 kV to establish comparisons between the potential different thicknesses of the

Table 1 Chemical composition of the AM1 single-crystal nickel-based superalloy (data provided by Safran Aircraft Engines)

	Ni	Cr	Co	W	Mo	Al	Ti	Ta	Hf
at. %	Bal.	8.8	6.8	1.8	1.3	11.6	1.5	2.7	0.02
wt. %		7.6	6.7	5.6	2.0	5.2	1.2	8.0	0.05

corrosion products. The cross-sections were made by mounting the samples in a phenolic resin and then polishing them to a 1 µm finish using a diamond paste. Special care was taken to prepare the cross-sections with waterless polishing and cleaning with absolute ethanol to prevent the dissolution of corrosion products. To reveal the microstructure of the substrates, an oxalic acid $H_2C_2O_4$ (10% vol.) etching was performed at 4 V for a few seconds. The positive and negative poles of the electrode are in contact with the metal and the oxalic acid solution, respectively.

Results and Discussion

Isothermal Oxidation

Figure 1-a shows the specific mass change (Δm/S) with its standard deviation as a function of time at 750 °C for AC AM1 and FHT AM1. Both curves increase rapidly in the early stages of oxidation before slowing down and stabilizing at 10 and 24 h, respectively. However, there is a difference with a slightly more significant increase in mass for AC AM1 after 240 h of oxidation, indicating a more pronounced oxide growth. To better detail these variations, the linear k_l and parabolic k_p oxidation constants were calculated using the complete law [24]. The values presented in the table embedded in Fig. 1-a consistently confirmed previous observations, revealing higher linear and parabolic rate constants for the AC material. The Arrhenius plot of the k_p values vs. the reciprocal temperature (Fig. 1-b) clearly show that the parabolic rate constant of the AC and FHT AM1 superalloys tends to decrease with decreasing temperature and that the difference in k_p between AC AM1 and FHT AM1 is more pronounced at 750 °C than at higher temperatures [22]. By comparing with the work of Brumm and Grabke for NiAl with and without Cr [25], our experimental k_p

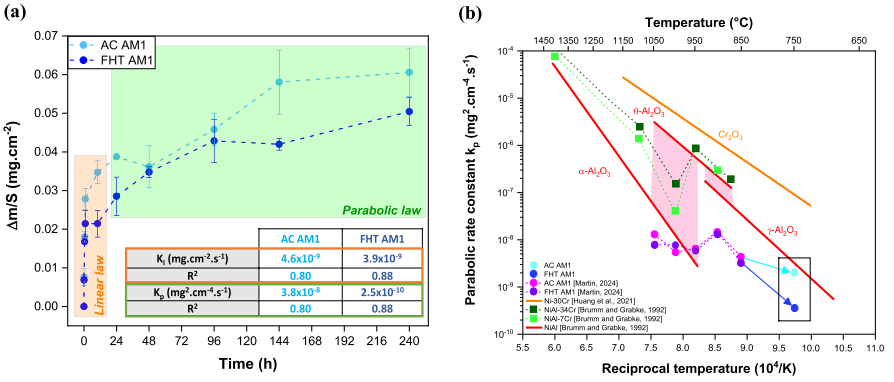

Fig. 1 **a** Mass gain per unit area of AM1 oxidized at 750 °C in air for 240 h as a function of time with a table gathering the different linear and parabolic domains (represented on the graph by the coloured rectangles) and **b** the graphical representation of Arrhenius' law integrating the parabolic kinetic constant k_p of AM1 oxidized in air at 750 °C for 240 h and various relative data from the literature, i.e., the isothermal oxidation of AC AM1 and FHT AM1 [22], the polymorphs Al_2O_3 of NiAl [25] and the Cr_2O_3 of Ni-30Cr [28]

values fall between those for the metastable growth of Al_2O_3 (γ-Al_2O_3) and those for the stable phase of Al_2O_3 (α-Al_2O_3). Since the k_p value of AC AM1 is closer to that of the γ-Al_2O_3, one may speculate this is the major oxide. In contrast, a comparable share of the γ-Al_2O_3 and α-Al_2O_3 phases in FHT AM1 can be assumed because the k_p value lies between those of corresponding oxides. Yet, it will be shown later (Fig. 4) that no γ-Al_2O_3 is formed. Instead, the metastable θ-Al_2O_3 and the stable α-Al_2O_3 polymorphs grow on different locations of the alloy substrates. After a 240-h exposure period at 750 °C in air the formation of transient alumina phases is expected to predominate according to Garriga-Majo et al. [26]. However, the formation of the stable α-Al_2O_3 can be explained by the presence of Cr in the superalloy, which acts as a third element to promote the formation of α-Al_2O_3 [22, 25, 27].

The microstructural impact on oxidation can be readily shown in Fig. 2. Indeed, the surface images in Fig. 2-a show that the heterogeneous oxide growth occurs mostly during the early stages of oxidation (between 5 min and 1 h) and essentially at the dendrite level for AC AM1. This microstructural inhomogeneity is naturally not observed at the surface of the FHT AM1. In all cases, the scales are believed to be very thin because the polishing lines and the dendritic and interdendritic areas are readily shown. Figure 2-b gathers the EDS surface analyses on the different zones of the two materials. Except for the predominant contribution of oxygen (excluded in Fig. 2-b to account only for the metal contribution), the scales are rich in Ni, Cr and Al rather than with Co, Ti and Ta although the signal of the underlying substrate shall not be neglected given the very thin scales formed. Yet, the corresponding oxides of the main metallic elements were also observed by XRD (NiO) (not shown) and by Raman spectroscopy (NiO and $(Cr,Al)_2O_3$) (shown later in Fig. 5). However, since Cr has been shown to segregate further in the dendrites than in the interdendritic areas of the AC AM1 superalloy [22], it appears unclear at this stage why the oxides would be richer in Cr in the interdendritic zones. It can

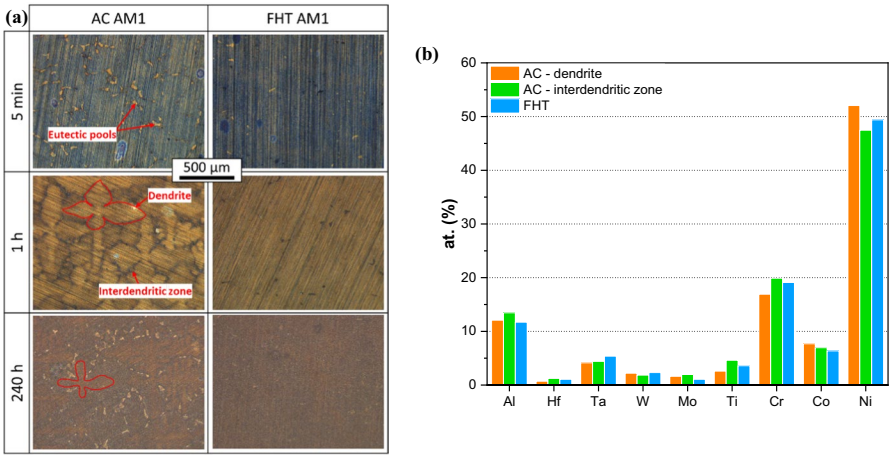

Fig. 2 **a** Optical microscopy images of the surface of the AC AM1 and FHT AM1 after various oxidation times and **b** comparative metallic contribution (in at. %) obtained by EDS performed at 20 kV on different areas of the surface after 240 h of oxidation in air at 750 °C

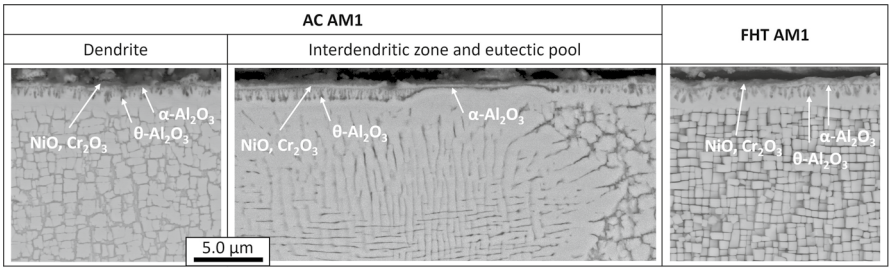

Fig. 3 Cross-sections of the AC (dendrite, interdendritic zone and eutectic pool) and of the FHT AM1 after oxidation in air for 240 h at 750 °C

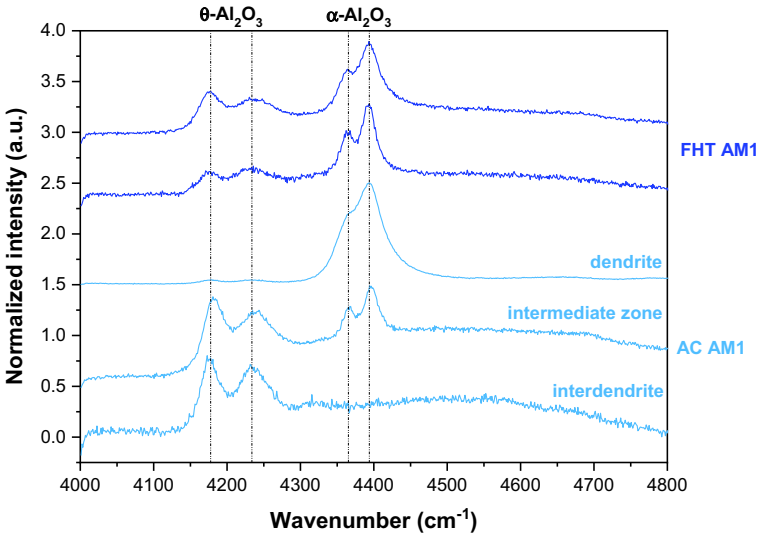

Fig. 4 Raman spectra in the fluorescence domain (with normalized intensity) of AC AM1 and FHT AM1 oxidized in air at 750 °C for 240 h

be hypothesized that a thicker layer of Ni oxide hinders Cr detection at the dendrite level. Alternatively, the oxide scale is thin on the interdendritic area, thus favouring detection of the γ'-depleted zone and/or the substrate. Cross-sections were thus performed to elucidate the oxidation mechanism of AM1 materials at this very low temperature of 750 °C (Fig. 3).

The three characteristic zones (dendrites, interdendritic zones and eutectic pools) of AC AM1 are clearly identified by slightly different oxidation attacks, although they all show a γ'-depleted zone below the oxide scale. Oxidation appears to be limited to certain areas of the eutectic pools, as shown in Fig. 3. However, except for these characteristic areas, the oxidation appears to be relatively similar involving internal oxidation in all cases. The complementary Raman analyses in different locations of the cross-section reveal two internal alumina phases (Fig. 4). For the

AC AM1 substrate, a metastable phase of θ-Al_2O_3 was mainly observed at the interdendritic zones, while in areas with a low volume fraction of γ' (dendrite), the stable α-Al_2O_3 phase is almost the only one to be formed despite the very high temperature or very long oxidation times required for its development [26]. Therefore, the formation of the α-Al_2O_3 phase in the dendritic areas is believed to occur because of the greater Cr content that favours Cr_2O_3 from which α-Al_2O_3 grows (third element effect) [22, 25]. The intermediate zones present both phases simultaneously, as does the entire surface of the FHT AM1. Complementary EDS analyses highlighted the presence of Al_2O_3 in regions with a large volume fraction of γ' with Ni and Cr oxides above (Fig. 3) in line with the observations of Perez et al. on the same FHT AM1 superalloy [27]. Although there are still some uncertainties about the chromium segregation in the interdendritic areas, there appears to be a preferential trend for chromia formation in areas with a reduced volume fraction of the γ' phase such as dendrites discussed earlier.

The oxidation processes of the γ/γ' structure of AM1-type superalloys can first be explained thermodynamically using the Ellingham diagram which takes into account the partial pressure of oxygen and temperature [29]. Aluminium requires the lowest oxygen partial pressure to form Al_2O_3 compared to the other superalloy elements. However, the kinetics and volume fraction of the γ' phase also influence the oxidation mechanisms. It is indeed observed the same type of successive layers on the different areas of the substrate, but with variable oxide levels. In particular, the internal oxidation (alumina formation) is observed to be greater in areas with a high fraction of γ' (interdendritic and eutectic zones) than in the dendritic zones (area with a lower fraction of γ'). Yet, the outer layer of NiO appears in the dendritic and interdendritic areas due to its relatively rapid diffusion at low temperatures [29, 30] but barely grows over the eutectic areas because of the coverage with Al_2O_3. The initial thickening of the NiO layer reduces the partial pressure of oxygen at the interface between the oxides and the substrate, favouring the external formation of chromium oxides (Cr_2O_3) and of aluminium oxides (Al_2O_3) in contact with the substrate. Such minor heterogeneities of the oxides growth at 750 °C have been ascribed to the different partitioning of the elements like chromium in other superalloy systems oxidized at higher temperatures [22, 30, 31].

Hot Corrosion by Na_2SO_4 Deposits

The addition of sodium sulphate to the surface of the two materials was then studied under the same experimental conditions as for oxidation at 750 °C under air for 240 h. The presence of salt on the surface of each sample limits the value of kinetics and surface analyses. The only relevant observations concern the change in the structure of Na_2SO_4 (from orthorhombic thenardite to trigonal aphthitalite) and the formation of traces of Na_2CrO_4 during the corrosion tests as observed by XRD (not given here) and Raman spectroscopy (Fig. 5) in line with the Raman results of other works [32, 33]. Then, similar peaks to those found under pure oxidation are observed in XRD and Raman, i.e. NiO and $(Cr,Al)_2O_3$. However, the oxide layer formed is very thin and the large number of elements in the AM1 superalloy make

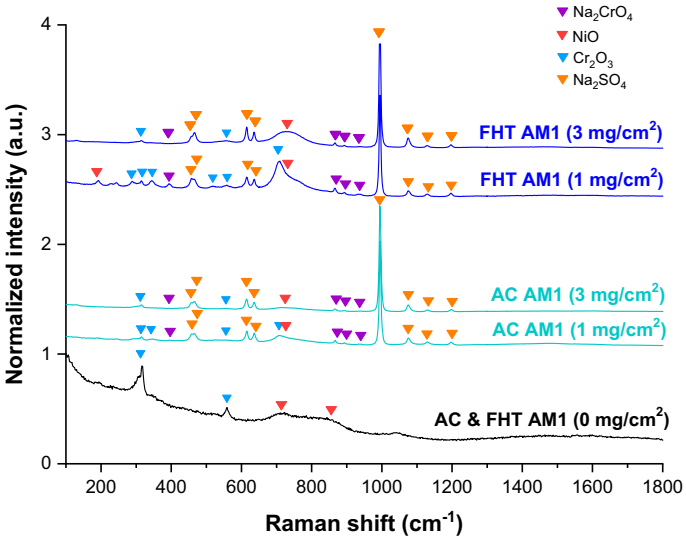

Fig. 5 Raman spectra (with normalized intensity) of AC AM1 and FHT AM1 oxidized (salt-free, 0 mg/cm^2) and corroded (with 1 and 3 mg/cm^2 of Na_2SO_4) in air at 750 °C for 240 h

the phase analysis difficult. It is possible that undetected phases correspond to other spinel or rutile phases associated with refractory elements (Ta, W, and Mo).

The cross-sections of the AC and FHT AM1 after the corrosion under deposits of 1 and 3 mg/cm^2 are shown in Fig. 6. It can be shown in Fig. 6a that a thicker corrosion layer grows with the smaller deposit of Na_2SO_4 irrespective the metallurgical area of the AC AM1. Such growth of the corrosion layer seems to be associated with

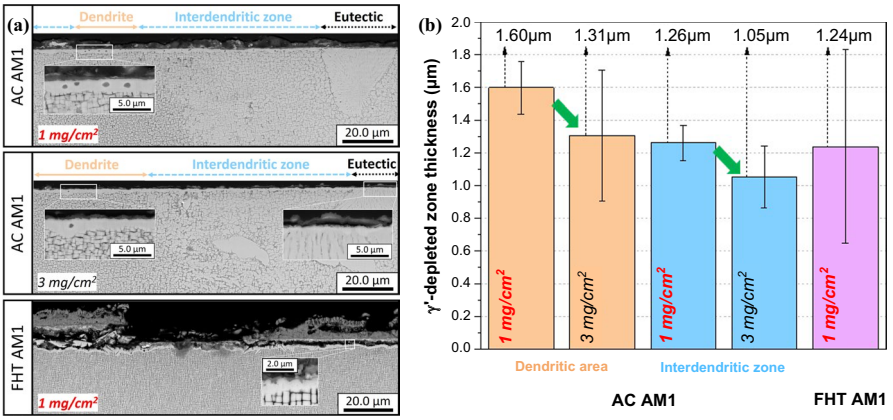

Fig. 6 **a** Cross-sections of AC AM1 and FHT AM1 corroded in air at 750 °C for 240 h with 1 and 3 mg/cm^2 including magnifications of representative areas and **b** graph showing the average thickness with standard deviation of the γ'-depleted zones, as a function of salt amount and specific metallurgical areas of the material

a relatively thicker γ'-depleted zone (Fig. 6). Furthermore, the depletion is more significant in the dendritic areas than in the interdendritic ones. Therefore, there is a clear effect of the chemical segregation on the corrosion of the AC AM1 material (eutectic vs. dendrite and interdendrites, see Fig. 7) as opposed to the FHT condition of the AM1 superalloy, which in turn grows a much thicker corrosion layer (about 10 µm) than the AC version (about 2 µm), which is indicative of a propagation step and detaches off the surface in different areas.

The higher magnification of Fig. 7 highlights that the dissolution of the outer γ'phase appears more marked with the decrease in the salt content in the AC condition but similar between the interdendritic AC and FHT given the greater initial γ' distribution. In addition, it is noteworthy that the formation of round-shaped sulphides is significantly higher with the 1 mg/cm^2 than with the 3 mg/cm^2 deposits and that they appear to be mainly concentrated in the low γ' volume fraction areas (dendritic areas in AC and in FHT). The sulphidation mechanism appears therefore to be the most harmful process in these tests despite the observation of internal oxidation at some locations. This suggests that in the absence of additional SO_2/SO_3 to the gas flow, the formation of the sulphides derives from the reactions, whereby sulphates decompose due to the reduction of P_{O2} upon the formation of NiO as follows: $SO_4^{2-} \rightarrow SO_3 + O^{2-}$, then $SO_3 \rightarrow SO_2 + 1/2\ O_2$ and finally, $SO_2 \rightarrow 1/2\ S_2 + O_2$ [34–36]. Then, the reaction of $(S_2 + M)$ gives different stoichiometries depending on the metal considered. Looking at the different effects (salt amount and microstructure), the attack turns out to be more pronounced for the material subjected to a complete heat treatment with a deposition of 1 mg/cm^2 including a marked propagation step.

Additional SEM–EDS analyses were performed for more accurate identification of degraded areas, and they were annotated directly on Fig.7. Chromium sulphide (CrS) is detected in all areas of the γ'-depleted zones. In addition, an Al depleted layer is identified at the interdendritic zones and eutectic pools suggesting two distinct regions separated by a front of tiny CrS precipitates. This boundary shows an

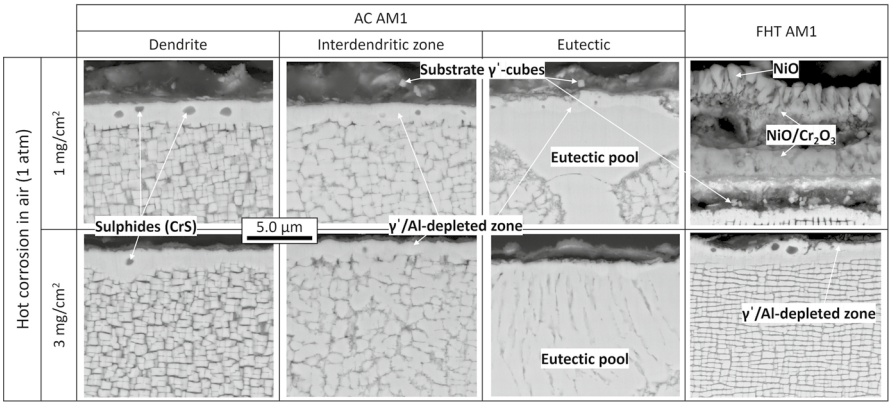

Fig. 7 High magnifications of Fig. 6-a showing the cross-sections of AC AM1 and FHT AM1 corroded in air at 750 °C for 240 h with 1 and 3 mg/cm^2 Na_2SO_4

upper zone depleted in aluminium and enriched in sulphur. This observation suggests that Na_2SO_4 decompose following the reactions given above and that the O_2 released induces oxidation in a first stage to develop an oxide layer through which sulphur is transported. Therefore, oxidation and sulphidation of the substrates occur in addition to basic fluxing assumed to occur, because Na_2CrO_4 has been detected (Fig. 5), without any contribution from SO_2/SO_3 flux. Progress of internal sulphidation has been reported to occur by the oxidation of Cr that promotes the release of S atoms that diffuse into the substrate [7]. The γ'-cubes embedded in the corrosion layers of the interdendritic and eutectic areas with 1 mg/cm^2 Na_2SO_4 (Fig. 7) are solely ascribed to the polishing process or electrochemical etching [37] but not to their dissolution since the Na_2SO_4 salt remained unmolten.

The analysis of the corrosion products of FHT AM1 indicates the formation of an outer layer of NiO, followed by a layer of oxides rich in Co and Cr, and an internal Al-rich layer, i.e., the same structure as with the pure oxidation, but the oxide layers are now far thicker. This is in line with the findings of Lortrakul et al. [38] when corroding CMSX-4 at 700 °C with Na_2SO_4 and $O_2/SO_2/SO_3$, i.e. under typical Type II hot corrosion conditions, they reported that the oxide scales grew much faster than in our case following two stages. The first one was related to the active corrosion through the eutectic Na_2SO_4-$NiSO_4$ although like in our case, they did not find any Ni and/or Co sulphate at the top. The second stage was governed by the SO_2/SO_3 mixture but they also claimed that the initial oxides had formed a barrier for the further attack of the S-containing gas and therefore, the gas had little influence. This also occurs with the increase in the amount of deposited salt from 1 to 3 mg/cm^2, which decreases surface degradation according to D.A. Shores who indicated that a thick film and a diluted SO_3 environment leads to basic conditions [39]. Despite the absence of the SO_2/SO_3 gaseous environment, this corrosion study indicates that the corrosion resistance of AC AM1 superalloy appears to be greater than that of FHT AM1, due to the protective Cr_2O_3 in areas characterized by a low volume fraction of γ ' that reacts under the present conditions to result in a Na_2CrO_4 (Fig. 5). The formation of Cr_2O_3 is assumed to occur very much like in the pure oxidation situation previously discussed.

Conclusions

The oxidation and hot corrosion of the A s- C ast (AC) and Fully Heat-Treated (FHT) AM1 single-crystal nickel-based superalloy were investigated at 750 °C in air (1 atm.) for 240 h. The main experimental observations lead to the following conclusions:

1. Under pure oxidation, a complex oxide layer is formed at 750 °C with mainly NiO, Cr_2O_3 and Al_2O_3. Depending on the volume fraction of γ', oxidation is more pronounced. The chemical segregation of the AC state enables more Cr_2O_3 to be formed in the dendrites (low fraction of γ') and more Al_2O_3 in the interdendritic and eutectic pools (high fraction of γ').

2. Hot corrosion at 750 °C can occur in single-crystal AM1 superalloy in the absence of SO_3 (g) flow given the sulphidation, oxidation and basic fluxing observed. This likely derives from the decomposition of the sulphate and then of the SO_x molecules producing S_2 and O_2. The increase in salt content decreases hot corrosive attack by forming a barrier layer to the external gas (air). Furthermore, the metallurgical segregations in the AC superalloy allow to extend the incubation period through the formation of a protective Cr_2O_3 layer like the one observed under pure oxidation in air.

Acknowledgements This work was partly funded by Safran Aircraft Engines under contract number 2500004896. The S-free AM1 alloy was provided by Safran Aircraft Engines. Special thanks to Prof. B. Grégoire at La Rochelle University and Prof. S. Mathieu at Lorraine University for fruitful discussion and reviewing the manuscript.

Author Contribution D. Piel involved in investigation, methodology, writing—original draft. A. Martin involved in supervision, validation, writing—original draft, writing—review and editing. E. Drouelle involved in supervision, validation. J. Cormier involved in supervision, Validation. F. Pedraza involved in methodology, investigation, writing—original draft, writing—review and editing.

Data Availability No datasets were generated or analysed during the current study.

Declarations

Conflict of interest The authors declare no competing interests.

References

1. E. Rahim, N. Warap, and Z. Mohid, Thermal-assisted machining of nickel-based alloy. in *Superalloys*. ed. Mahmood Aliofkhazraei (InTech, 2015).
2. D. A. Shifler. High-Temperature Corrosion in Military systems. In: Corrosion: environments and industries. Materials Park, Ohio: ASM International; 2006:13C:156–170
3. A. H. Mourad, A. Almomani, I. A. Sheikh, and A. H. Elsheikh, Failure analysis of gas and wind turbine blades: A review. *Eng. Failure Anal.* **146**, 2023 (107107).
4. J. A. Goebel and F. S. Pettit, Na_2SO_4-induced accelerated oxidation (hot corrosion) of nickel. *Metall. Trans.* **1**, 1970 (1943–1954).
5. F. Alten, Jr. Grandt. Fundamentals of Structural Integrity: Damage Tolerant Design and Non Destructive Evaluation. New York; 2004.
6. B. S. Lutz, G. R. Holcomb, and G. H. Meier, Determination of the initiation and propagation mechanism of fireside corrosion. *Oxid. Met.* **84**, 2015 (353–381).
7. M. K. Kumawat, C. Parlikar, M. D. Zafir Alam, and D. K. Das, Type-I hot corrosion of Ni-base superalloy CM247LC in presence of molten Na_2SO_4 film. *Metall. Mater. Trans. A.* **52**, 2021 (378–393).
8. G. H. Meier, A review of advances in high-temperature corrosion. *Mater. Sci. Eng. A.* **120**, 1989 (1–1).
9. K. L. Luthra, Low temperature hot corrosion of cobalt-base alloys: Part I morphology of the reaction product. *Metall. Trans. A* **13**, (10), 1982 (1843–1852).
10. K. L. Luthra, Low-temperature hot corrosion of cobalt-base alloys. Part II. reaction mechanism. *Metall. Trans.* **13A**, 1982 (1853–1864).
11. Y. Wang, R. Pillai, E. Yazhenskikh, M. Frommherz, M. Müller, and D. Naumenko, Role of temperature in Na_2SO_4–K_2SO_4 deposit induced type II hot corrosion of NiAl coating on a commercial Ni-based superalloy. *Adv. Eng. Mater.* **22**, (6), 2020 (1901244).

12. R. Malacarne, S. Mathieu, L. Aranda, et al., Type II hot corrosion of A718 and AD 730™ polycrystalline Ni-based alloys: influence of the SO_3 partial pressure. *Corros. Sci.* **224**, 2023 (111550).
13. G. Cailletaud and G. Eggeler, Foreword: Ni-base superalloy single crystals, a fascinating class of high temperature engineering materials. in *Nickel Base Single Crystals Across Length Scales*, (Elsevier, 2022), pp. xiii–xvii.
14. R. Malacarne, S. Mathieu, M. Siblani, et al., On the sulfation reaction of protective and transient oxides at 650 °C and its role in the low temperature hot corrosion mechanism. *Corros. Sci.* **218**, 2023 (111186).
15. K. P. Lillerud and P. Kofstad, Sulfate-induced hot corrosion of nickel. *Oxid. Met.* **21**, 1984 (233–270).
16. K. L. Luthra and D. A. Shores, Mechanism of Na_2SO_4 induced corrosion at 600–900 °C. *J. Electrochem. Soc.* **127**, 1980 (2202–2210).
17. J. Stringer, High-temperature corrosion of superalloys. *Mater. Sci. Technol.* **3**, 1987 (482–493).
18. S. Hu, Y. Zhao, W. Bai, et al., Orientation control for nickel-based single crystal superalloys: grain selection method assisted by directional columnar grains. *Materials.* **15**, 2022 (4463).
19. P. Caron. Le développement des superalliages monocristallins à base de nickel. Journées Annuelles de la SF2M, 2016;
20. C. Tabata, T. Osada, T. Yokokawa, A. Ikeda, K. Kawagishi, and S. Suzuki, Effect of solution heat-treatment on the oxidation resistance of Ni-base single-crystal superalloy. *Metall. Mater. Trans. A.* **54**, 2023 (4825–4833).
21. S. Pierret, T. Etter, A. Evans, and H. Van Swygenhoven, Origin of localized rafting in Ni-based single crystal turbine blades before service and its influence on the mechanical properties. *Acta Mater.* **61**, 2013 (1478–1488).
22. A. Martin, J. Cormier, J. Rame, E. Drouelle, and F. Pedraza, Influence of microstructure on the oxidation behaviour of the Ni-based single crystal superalloy AM1 between 850 and 1050 °C in air. *Corros. Sci.* **229**, 2024 (111872).
23. ISO 17224:2015: Corrosion of metals and alloys - Test method for high temperature corrosion testing of metallic materials by application of a deposit of salt, ash, or other substances.
24. D. Monceau and B. Pieraggi, Determination of parabolic rate constants from a local analysis of mass-gain curves. *Oxid. Met*. **50**, 1998 (477–493).
25. M. W. Brumm and H. J. Grabke, The oxidation behaviour of NiAl-I. Phase transformations in the alumina scale during oxidation of NiAl and NiAl-Cr alloys. *Corros. Sci*. **33**, (11), 1992 (1677–1690).
26. D. P. Garriga-Majo, B. A. Shollock, D. S. McPhail, R. J. Chater, and J. F. Walker, Novel strategies for evaluating the degradation of protective coatings on superalloys. *Int. J. Inorg. Mater.* **1**, (5–6), 1999 (325–336).
27. T. Perez, D. Monceau, and C. Desgranges, Kinetic oxidation model including the transient regime for a single crystal nickel-based superalloy over the temperature range 750–1300 °C. *Corros. Sci.* **206**, 2022 (110485).
28. X. Huang, L. Martinelli, S. Bosonnet, P. C. M. Fossati, L. Latu-Romain, and Y. Wouters, Effect of temperature on the oxidation mechanism of Ni-30Cr alloy. *Oxid. Met.* **96**, 2021 (69–78).
29. M. Onillon, J. Perrin. Les diagrammes d'Ellingham et les équilibres oxydes-phase gazeuse. L'Actualité Chimique. 1978 (33–38).
30. A. Sato, Y.-L. Chiu, and R. C. Reed, Oxidation of nickel-based single-crystal superalloys for industrial gas turbine applications. *Acta Mater.* **59**, 2011 (225–240).
31. J. Pistor, S. P. Hagen, S. Virtanen, and C. Körner, Influence of the microstructural homogeneity on the high-temperature oxidation behavior of a single crystalline Ni-base superalloy. *Scripta Mater.* **207**, 2022 (114301).
32. N. Prieto-Taboada, S. Fdez-Ortiz de Vallejuelo, M. Veneranda, et al. The Raman spectra of the Na_2SO_4-K_2SO_4 system: Applicability to soluble salts studies in built heritage. *J. Raman Spectrosc*. 2019;50 (175–183)
33. J. E. D. Davies and D. A. Long, Solid-state vibrational spectroscopy. part II. The vibrational spectra of some chromates and dichromates. *J. Chem. Soc. A: Inorg. Phys., Theor.* 1971.
34. B. Grégoire, X. Montero, M. C. Galetz, G. Bonnet, and F. Pedraza, Mechanisms of hot corrosion of pure nickel at 700 °C: influence of testing conditions. *Corros. Sci*. **141**, 2018 (211–220).
35. J. Tjandra, A. Ranjan, A. K. Ackerman, M. Appleton, and S. Pedrazzini, Effect of NaCl and Na_2SO_4 on low temperature corrosion of vapour- and pack-aluminide coated single crystal turbine blade alloys CMSX-4 and RR3010. *Metall. Mater. Trans. A*. **54**, 2023 (3286–3299).

36. T. Gheno and B. Gleeson, on the hot corrosion of nickel at 700 °C. *Oxid. Met.* **84**, 2015 (567–584).
37. R. Salehi, A. Samadi, and MKh. Savadkoohi, Influence of etchants on quantitative/qualitative evaluations of the γ' precipitates in a nickel-base superalloy. *Metallogr. Microstruct. Anal.* **1**, 2012 (290–296).
38. P. Lortrakul, R. W. Trice, K. P. Trumble, and M. A. Dayananda, Investigation of the mechanisms of Type-II hot corrosion of superalloy CMSX-4. *Corros. Sci.* **80**, 2014 (408–415).
39. D. A. Shores. High Temperature Corrosion. R. A. Rapp, Ed., National Association of Corrosion Engineers, *Houston*, Texas. 1983;493.